How AGN and SN Feedback Affect Mass Transport and Black Hole Growth in High-redshift Galaxies

Joaquin Prieto[1], Andrés Escala[1], Marta Volonteri[2], and Yohan Dubois[2]

[1] Departamento de Astronomía, Universidad de Chile, Casilla 36-D, Santiago, Chile

[2] CNRS and UPMC Université Paris 06, UMR 7095, Institut d'Astrophysique de Paris, 98 bis Boulevard Arago, Paris F-75014, France

Abstract

Using cosmological hydrodynamical simulations, we study the effect of supernova (SN) and active galactic nucleus (AGN) feedback on the mass transport (MT) of gas onto galactic nuclei and the black hole (BH) growth down to redshift $z \sim 6$. We study the BH growth in relation to the MT processes associated with gravity and pressure torques and how they are modified by feedback. Cosmological gas funneled through cold flows reaches the galactic outer region close to freefall. Then torques associated with pressure triggered by gas turbulent motions produced in the circumgalactic medium by shocks and explosions from SNe are the main source of MT beyond the central $\sim$100 pc. Due to high concentrations of mass in the central galactic region, gravitational torques tend to be more important at high redshift. The combined effect of almost freefalling material and both gravity and pressure torques produces a mass accretion rate of order $\sim 1\, M_\odot\, \mathrm{yr}^{-1}$ at approximately parsec scales. In the absence of SN feedback, AGN feedback alone does not affect significantly either star formation or BH growth until the BH reaches a sufficiently high mass of $\sim 10^6\, M_\odot$ to self-regulate. SN feedback alone, instead, decreases both stellar and BH growth. Finally, SN and AGN feedback in tandem efficiently quench the BH growth, while star formation remains at the levels set by SN feedback alone, due to the small final BH mass, $\sim$few times $10^5\, M_\odot$. SNe create a more rarefied and hot environment where energy injection from the central AGN can accelerate the gas further.

Key words: galaxies: formation – large-scale structure of the universe – quasars: supermassive black holes – stars: formation – turbulence

1. Introduction

There is dynamical evidence for the existence of supermassive black holes (BHs) in the center of many nearby galaxies (Ferrarese & Ford 2005) with masses in the range $M_{\mathrm{BH}} \sim 10^6$–$10^9\, M_\odot$, suggesting that BHs, formed at the first evolutionary stages of our universe, now are living in the galactic centers around us, including our Galaxy (Ghez et al. 2005).

Scaling relations connect the masses of BHs in local galaxies with their host galaxy properties, such as the galactic bulge mass (e.g., Magorrian et al. 1998; Gültekin et al. 2009) and the bulge stars' velocity dispersion (e.g., Ferrarese & Merritt 2000; Tremaine et al. 2002). Such relations suggest a coevolution between the BH and its host galaxy (see, e.g., Dressler 1989; Kormendy & Richstone 1995; Magorrian et al. 1998; Gebhardt et al. 2000), with a recent work suggesting that such a coevolution can be triggered in galactic bulges with a critical mass above $\sim 10^6\, M_\odot$ in the early stages of galactic evolution (Park et al. 2016).

Detection of very bright quasars at redshift $z \gtrsim 6$ with luminosities above $10^{13}\, L_\odot$ implies the existence of BHs with masses of the order $M_{\mathrm{BH}} \sim 10^9\, M_\odot$ when our universe was $\sim$1 Gyr old (Fan et al. 2001; Willott et al. 2007; Mortlock et al. 2011; De Rosa et al. 2014), i.e., BHs should have formed very early in the history of our universe and grown rapidly in order to attain such high masses after $\sim$1 Gyr (Dubois et al. 2012; Di Matteo et al. 2012, 2016). Understanding such a rapid early evolution is one of the main challenges of the current galaxy formation theories (Volonteri 2010; Haiman 2013).

In previous work, Prieto & Escala (2016, hereafter PE16) have studied the mass transport (MT) process in high-redshift galactic disks focusing on the effect of supernova (SN) feedback without taking into account active galactic nucleus (AGN) activity on such objects. They show that SN feedback is able to affect dramatically the BH growth in the first galaxies at high redshift (see also Dubois et al. 2015; Bower et al. 2016; Habouzit et al. 2016).

As in PE16, we study the evolution of a high-redshift galaxy. In particular, we compute internal dynamical properties of the system to study the effect of AGN activity in the MT process in galactic disks at redshift $z \gtrsim 6$. Outflows generated by AGN activity can have spatial extensions of at least $\sim$1 kpc and can reach velocities of the order of $\sim 10^3\, \mathrm{km\, s}^{-1}$ (e.g., Humphrey et al. 2010; Nesvadba et al. 2011; Arribas et al. 2014; Genzel et al. 2014). Such powerful outflows should be capable of affecting the host galaxy evolution and the BH growth. We explore the individual effects of SNe and AGNs in galaxy evolution, and, furthermore, we study how super-Eddington accretion may affect the system.

The paper is organized as follows. Section 2 contains the numerical details of our simulations. In Section 3 we present our results based on the gas dynamic analysis of our simulations and its effect on BH growth. In Section 4 we discuss the results and present our main conclusions.

2. Methodology and Numerical Simulation Details

The simulations analyzed in this paper are an extension of the work presented in PE16, with a few modifications. Therefore, we briefly recall the physical ingredients of the numerical experiments.

The simulations were performed with the cosmological N-body hydrodynamical code RAMSES (Teyssier 2002). The code uses adaptive mesh refinement and solves the Euler equations with a second-order Godunov method and MUSCL

scheme using a MinMod total variation diminishing scheme to reconstruct the cell-centered values at cell interfaces.

Cosmological initial conditions were generated with the MPGRAFIC code (Prunet et al. 2008) inside an $L = 10$ cMpc (co-moving Mpc) side box. Cosmological parameters were taken from Planck Collaboration (2013), with total matter density $\Omega_m = 0.3175$, dark energy density $\Omega_\Lambda = 0.6825$, baryon matter density $\Omega_b = 0.04899$, reduced Hubble parameter $h = 0.6711$, amplitude of the power spectrum at a scale of 8 h^{-1} Mpc $\sigma_8 = 0.83$, and spectral index $n_s = 0.9624$.

We have selected a $3 \times 10^{10}\,M_\odot$ dark matter (DM) halo at $z = 6$ to be resimulated at high resolution from $z_{ini} = 100$ to $z_{end} = 6$. The high-resolution particles have mass $m_{part} \approx 3 \times 10^4\,M_\odot$ (which corresponds to an effective resolution of 1024^3 DM particles inside the box). Such a mass allows us to resolve our final halo with $\sim 10^6$ DM particles. In order to resolve all the interesting regions, we allowed refinements inside the Lagrangian patch associated with a sphere of radius $R_{ref} = 3\,R_{vir}$ around the selected DM halo at z_{end} (here R_{vir} is the DM halo virial radius, defined as the radius associated with a spherical overdensity 200 times that of the mean matter density of the universe at the corresponding redshift). The Lagrangian volume (the mask) is defined by an additional scalar advected passively with the flow throughout the simulation. At the beginning the passive scalar has a value equal to 1 inside the mask and 0 outside. In regions where this passive scalar is larger than 10^{-3} we allow refinement in a cell if any of these conditions are met: (i) its total mass is more than 8 times that of the initial mass resolution, (ii) the Jeans length is resolved by less than 4 cells (Truelove et al. 1997), or (iii) the relative pressure variation between cells is larger than a factor of 2. Following these criteria, we reach a maximum comoving spatial resolution of $\Delta x_{min} \approx 38.1$ cpc and a proper spatial resolution of $\Delta x_{min} \approx 5.4$ pc at redshift z_{end}, whereas the coarse grid inside the mask has a resolution of $\Delta x_{coarse} \approx 9.8$ ckpc. The gravitational force resolution is Δx_{min} throughout the simulation.

Our simulations include optically thin (no self-shielding) gas cooling following the Sutherland & Dopita (1993) model down to temperature $T = 10^4$ K with a contribution from metals, assuming a primordial composition of the various heavy elements. Below this temperature, the gas can cool down to $T = 10$ K, due to metal line cooling (Dalgarno & McCray 1972). We started the simulations with an initial metallicity of $Z_{ini} = 0.001\,Z_\odot$ (Powell et al. 2011). A uniform UV background is activated at $z_{reion} = 8.5$, following Haardt & Madau (1996).

We adopted a star formation number density threshold of $n_0 \approx 30$ H cm^{-3} with a star formation efficiency $\epsilon_\star = 0.05$ (e.g., Rasera & Teyssier 2006; Dubois & Teyssier 2008). When a cell reaches the conditions for star formation, star particles can be spawned following a Poisson distribution with a mass resolution of $m_{\star,res} \approx 5 \times 10^4\,M_\odot$. In order to ensure numerical stability, we do not allow conversion of more than 50% of the gas into stars inside a cell in one time step.

After 10 Myr, the most massive stars explode as SNe releasing a specific energy of $E_{SN} = 10^{50}$ erg/$M_\odot$, returning 10% of the stellar particle mass back into the gas and with a yield of 0.1 inside a sphere of $r_{SN} = 2\Delta x_{min}$. As in PE16, we used the delayed cooling implementation of SN feedback (Teyssier et al. 2013). This means that, where SNe explode, if the gas "nonthermal" energy (stored in a separate passive variable) is above an energy threshold e_{NT}, gas cooling is turned off in order to take into account the

unresolved chaotic turbulent energy source of the explosions. This nonthermal energy component dissipates energy at its own rate with characteristic time t_{diss}. In this work (as in PE16) we use $t_{diss} = 0.5$ Myr, and the energy threshold e_{NT} is the one associated with a turbulent velocity dispersion $\sigma_{NT} = 50$ km s^{-1} through the equation $e_{NT} = \rho\sigma_{NT}^2/2$, with ρ the gas density. Such a velocity dispersion is appropriate for our spatial resolution (see Dubois et al. 2015; Prieto & Escala 2016, for details).

In order to follow the evolution of the central BH in the simulations, we introduced a sink particle (Bleuler & Teyssier 2014) when the main DM halo has a mass $M_h \approx 1.7 \times 10^8\,M_\odot$ at redshift $z = 15.7$. The BH seed mass is $10^4\,M_\odot$. Such a BH mass is in the range of masses associated with the direct collapse scenario (e.g., Oh & Haiman 2002; Begelman et al. 2006, 2008; Lodato & Natarajan 2006; Agarwal et al. 2012; Latif et al. 2013, 2014; Choi et al. 2015). Only this one single BH is allowed to form in the simulation.

In order to compute the mass accretion rate onto the BH, we use the standard Bondi–Hoyle (Bondi 1952) implementation of the accretion rate, $\dot{M}_{Bondi}$. In all our simulations except for one, we cap the accretion rate at the Eddington luminosity. For more details on the numerical implementation of the processes described above, see PE16.

In order to avoid spurious oscillations in the sink position, we have introduced a drag force acting on the BH particle (Biernacki et al. 2017). The drag force comes from a new source of momentum acting on the sink. Such a momentum variation is proportional to the cell gas-sink particle relative velocity. Furthermore, it depends on the nonaccreted mass above the Eddington limit: when the BH accretion rate is below the Eddington limit, the drag force is null; it works only if the Bondi BH mass accretion rate is above the Eddington limit. In this sense it can be interpreted as a force associated with the Eddington pressure around the BH particle. In the simulation where accretion is not capped at the Eddington limit, there is no drag force. However, even in this extreme case the sink particle stays at the center of the galaxy.

We have also included AGN feedback from the BH. AGN feedback is modeled with thermal energy input (Teyssier et al. 2011; Dubois et al. 2012). The rate of energy deposited by the BH inside the injection radius $r_{inj} \equiv 4\Delta x_{min}$ is

$$\dot{E}_{AGN} = \epsilon_c\,\epsilon_r\,\dot{M}_{BH}c^2. \quad (1)$$

In the above expression, $\epsilon_r = 0.1$ is the radiative efficiency for a standard thin accretion disk (Shakura & Sunyaev 1973), and $\epsilon_c = 0.15$ is the fraction of this energy coupled to the gas in order to reproduce the local BH–galaxy mass relation (Dubois et al. 2012). As explained in Booth & Schaye (2009), in order to avoid gas overcooling, the AGN energy is not released instantaneously every time step Δt, but it is accumulated until the surrounding gas temperature can be increased by $\Delta T_{min} = 10^7$ K. The time between the energy injection events depends on the BH mass, mean gas density, and mass accretion rate. It is $\Delta t_{AGN} \sim 1$–100 kyr in our simulations.

3. Results

In this work we will show results from four simulations:

1. SNe run: it includes star formation, SN feedback, and modified Bondi–Hoyle–Lyttleton accretion rate onto
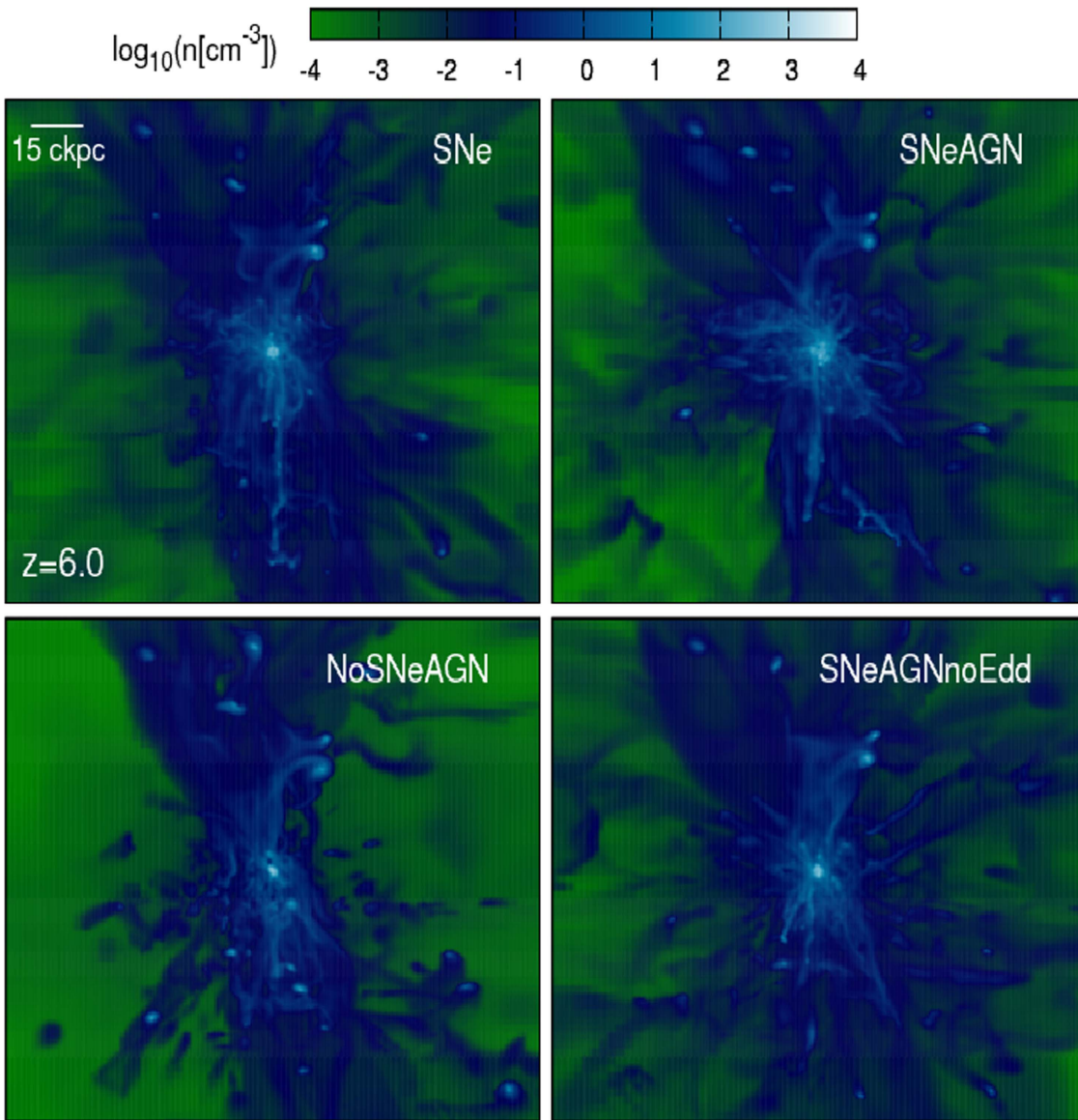
Figure 1. Gas number density projections for the four experiments at the end of the runs. Each panel has an extension of ∼120 ckpc. It is interesting to note that the SNeAGN experiment presents a galaxy much more extended compared with the NoSNeAGN simulation, where a dense central knot is surrounded by low-density gas. Such a morphological difference shows how important the SN heating is for creating a rarefied environment where the AGN feedback can work much more efficiently.

sinks without AGN feedback. This case was extensively analyzed in PE16, and here we compare it with our AGN simulations.

2. SNeAGN run: same as the SNe run plus AGN feedback.
3. NoSNeAGN run: same as the SNeAGN run but without SN feedback.
4. SNeAGNnoEdd run: same as the SNeAGN run but without capping at the Eddington limit.

Figure 1 shows the gas number density projection for the four simulations at the end of the experiments. Each panel presents different features depending on the different feedback recipes, as will be explained in the following sections.

3.1. Mass Transport on Large Scales

Because in a cosmological context at high redshift we cannot study the small galactic scale phenomena without taking into account the effects of the large-scale structure, here we study the behavior of mass accretion from roughly a few hundred parsecs up to ∼$3R_{\mathrm{vir}}$, with R_{vir} the DM halo virial radius.

Figure 2 shows the mass accretion rate, computed taking into account all the gas mass crossing a spherical shell at a given radius centered at the sink cell position:

$$\frac{dM_{\mathrm{g}}}{dt} = -4\pi r^2 \rho v_r, \qquad (2)$$

where ρ is the gas mass density and v_r is the total radial gas velocity.

The left column of Figure 2 shows the total gas mass accretion rate for our four simulations as a function of radius. The right column shows instead the mass accretion rate associated with low gas density $\rho_{\mathrm{coll}} = 18\pi^2\Omega_{\mathrm{b}}\rho_{\mathrm{c}} \approx 200\Omega_{\mathrm{b}}\rho_{\mathrm{c}}$, with ρ_{c} the critical density of the universe. For the redshift range shown in the figure, $\rho_{\mathrm{coll}} \approx (2\text{–}7) \times 10^{-2}\,\mathrm{cm}^{-3}$. This range of densities is below the mean baryon density in cold
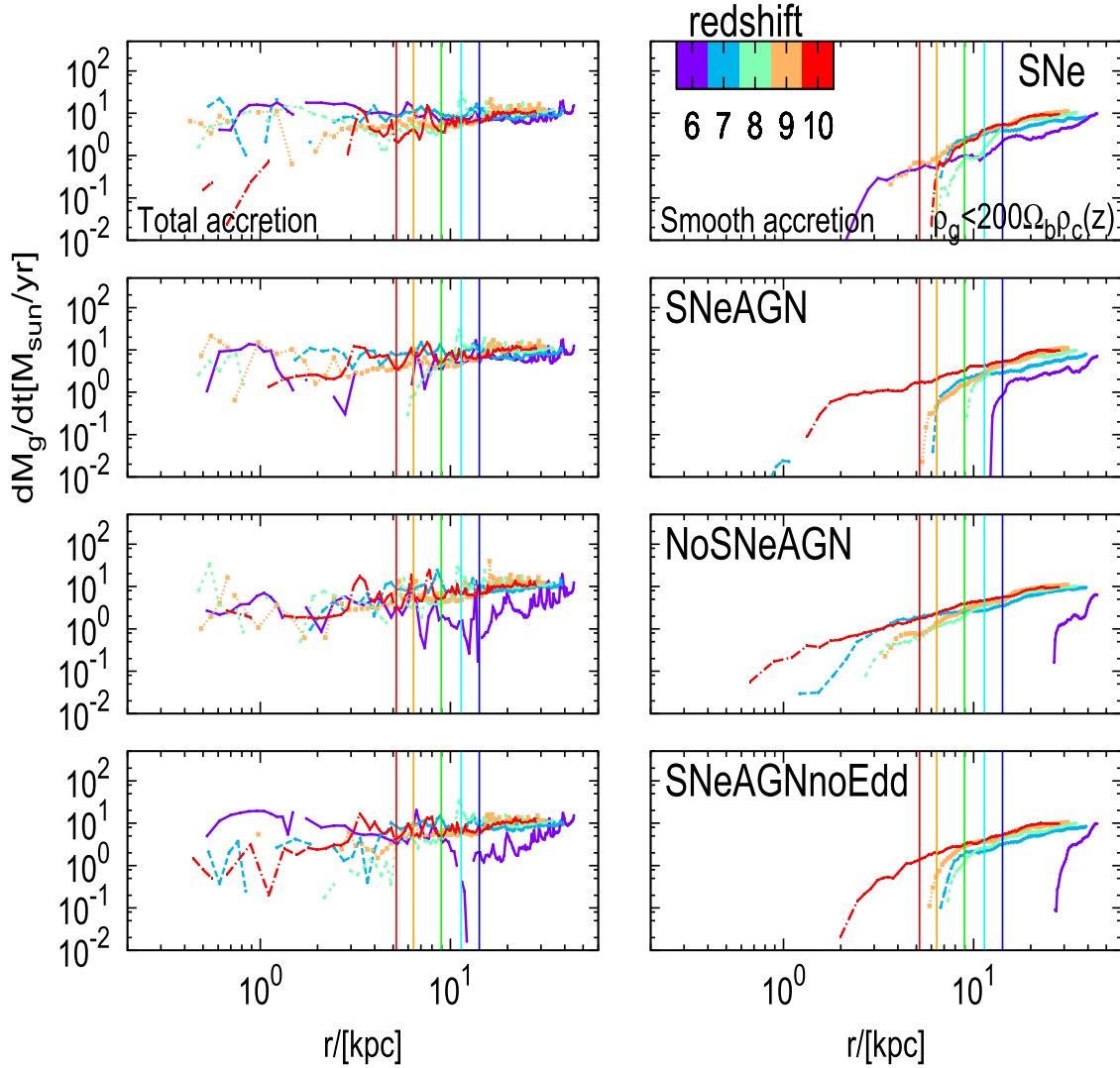
Figure 2. Left column: total gas mass accretion rate as a function of radius for our different runs at different redshifts, $z = 10$ in red, $z = 9$ in orange, $z = 8$ in green, $z = 7$ in cyan, and $z = 6$ in blue. From top to bottom: SNe, SNeAGN, NoSNeAGN, and SNeAGNnoEdd. Right column: same as the left column, but for low-density smooth accretion, i.e., for gas with a density below the collapse density $\rho_g < 200\Omega_b\rho_c$. Beyond the virial radius (marked as vertical lines) the total mass accretion rate has a floor similar to the smooth accretion: roughly a few tens of $M_\odot$ yr^{-1}. Inside the virial radius the accretion rate is dominated by dense $n \lesssim 10^3$ cm^{-3} gas.

flows in our simulations, which is ~1–0.1 cm^{-3}. The vertical lines mark the DM virial radius at each sampled redshift.

Beyond the virial radius all our simulations show a mass accretion rate of ~10 $M_\odot$ yr^{-1}, in agreement with PE16. This mass accretion rate is associated with gas almost freefalling onto the DM halo. At these radii the inflowing material is dominated by gas with densities $n \sim 1$–0.1 cm^{-3}. Those are characteristic densities in cooling flows. This quantity shows peaks (~few tens of $M_\odot$ yr^{-1}) associated with both gas clumps and DM minihalos inside the virial radius. From the right column, we see how feedback suppresses low-density ($n \sim 10^{-2}$ cm^{-3}) gas accretion inside the inner ~1 kpc. Because of the feedback heating, only the densest gas is able to flow into the galactic central region. At the end of the simulations, gas with densities $n \sim 1$–0.1 cm^{-3} can reach the outer galactic region (~0.1$R_{\rm vir}$) but not beyond, because it is heated and expelled from the galaxy. When we include material with density below 10 cm^{-3}, it can penetrate the galaxy, but it cannot reach the central ~few times 10^2 pc. Only the densest gas can reach the galactic central region: material with density

below ~100 cm^{-3} is able to reach the central ~few times 10^2 pc region.

The AGN simulations show that at $z = 6$ the low-density material cannot penetrate inside the virial radius. By this time, AGN activity is capable of evaporating the diffuse material. At higher redshift the diffuse gas can reach smaller radii, but the accreted material is dominated by high-density gas. In particular, our NoSNeAGN simulation has the deepest low-density gas penetration at $z \geqslant 7$. In this case, due to the no SN heating and the low BH mass (few times $10^6 M_\odot$), AGN feedback is unable to alter significantly the low-density ~kiloparsec-scale accretion. At lower redshift the BH experiences a prolonged Eddington-limited accretion rate (as discussed in the following) that increases its mass by a factor of roughly a few, injecting in turn energy into the interstellar and circumgalactic media. Such energy injection clearly affects the low-density gas accretion rate at $z = 6$, as we can see from the figure: the low-density gas barely reaches the virial radius.

We note that the expression in Equation (2) includes mass inflows associated with inward radial motions triggered by local thermal fluctuations. In order to asses how important are
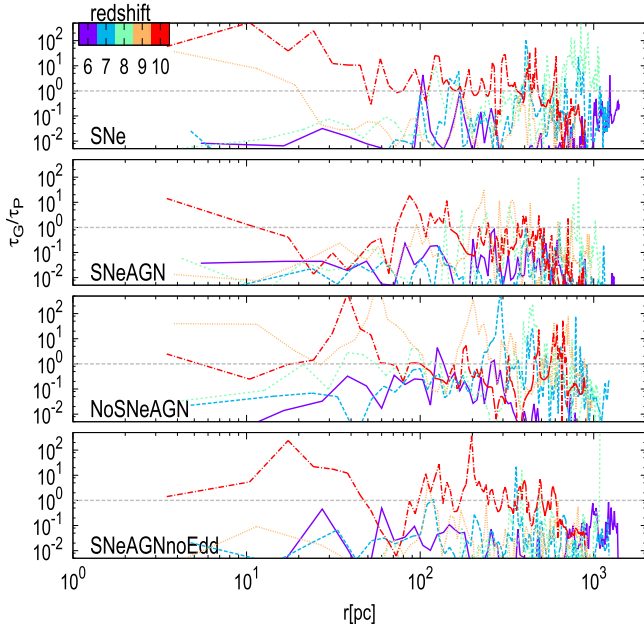
Figure 3. Ratio of gravitational torque to pressure gradient torque as a function of radius for different redshifts: $z = 10$ in red, $z = 9$ in orange, $z = 8$ in green, $z = 7$ in cyan, and $z = 6$ in blue. The ratio is smoothed over ~ 30 pc in radius. From top to bottom: SNe, SNeAGN, NoSNeAGN, and SNeAGNnoEdd. The gray dashed line marks the $\tau_G/\tau_P = 1$ state. Above ~ 100 pc the systems tend to be dominated by pressure gradient torques. Despite that, gravitational torques are also effective at $r \gtrsim 100$ pc in some regions. The no-SN-feedback simulations show a higher gravitational contribution below $r \gtrsim 100$, due to the lack of SN heating.
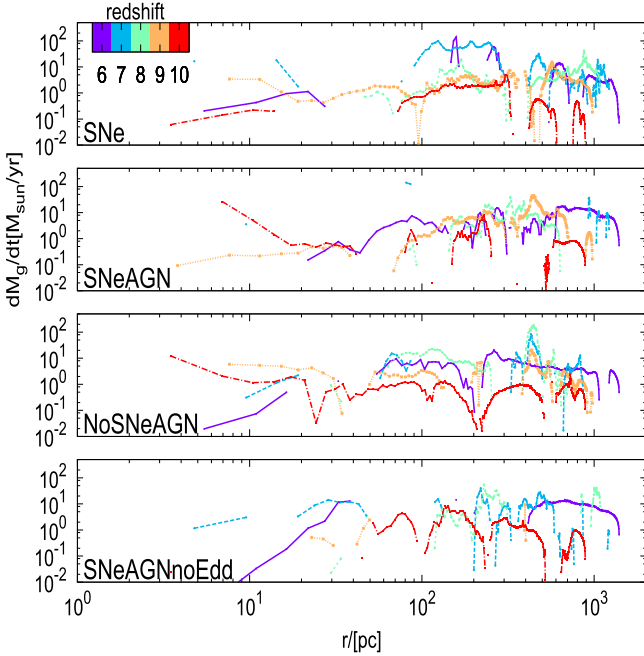

Figure 4. Mass accretion rate radial profiles inside $0.1\,R_{\mathrm{vir}}$ for our four runs at different redshifts: $z = 10$ in red, $z = 9$ in orange, $z = 8$ in green, $z = 7$ in cyan, and $z = 6$ in blue. All simulations show fluctuations in the mass accretion rate with values between $\sim 10^2$ and $\sim 10^{-2}\,M_{\odot}\,\mathrm{yr}^{-1}$. Due to the lack of SN heating, the NoSNeAGN run has the smoother data at high redshift.

the local thermal fluctuations to the mass accretion rate, we compute the radial velocity dispersion $\sigma_{r,\mathrm{NoSNe}}$ in the no-feedback simulation of PE16. Then, for each simulation presented in this work, we compute the mass accretion rate

including all the material with radial velocity

$$|v_r| > \sqrt{\sigma_{r,\mathrm{NoSNe}}^2}, \tag{3}$$

i.e., we excluded local thermal fluctuations. Following this procedure, we can see that at roughly virial radius scales the local velocity fluctuations are no more than $\sim 20\%$ of the total accreted matter.

The total mass accretion rate in our four simulations has similar values at roughly kiloparsec scales fluctuating between $\lesssim 10^{-1}\,M_{\odot}\,\mathrm{yr}^{-1}$ and $\sim$few tens of $M_{\odot}\,\mathrm{yr}^{-1}$, showing that the effect of the AGN activity does not have a notable impact on roughly kiloparsec scales in these small high-redshift galaxies, due to the small BH mass. Such accretion rates of order $\sim$few tens of $M_{\odot}\,\mathrm{yr}^{-1}$ at the outer galactic edge are associated with freefall material reaching the central DM halo region from large scales, as discussed in PE16.

3.2. Mass Transport in the Disk

The tight relation between the large-scale $\gtrsim R_{\mathrm{vir}}$ dynamic and the small-scale $\lesssim R_{\mathrm{vir}}$ evolution in the galaxy formation context (e.g., Pichon et al. 2011; Dubois et al. 2012; Danovich et al. 2015; Prieto et al. 2015) is a robust motivation to study the MT process at different scales in the first galaxies. In the following, we analyze the MT process on less than or approximately kiloparsec ($\lesssim 0.1\,R_{\mathrm{vir}}$) scales.

3.2.1. Torques in the Disk

After to inflow almost at freefall from scales above $\sim R_{\mathrm{vir}}$ until the galactic edge (at $\sim 0.1 R_{\mathrm{vir}}$) triggered by gravity and channelized through DM filaments around the DM halo, the angular momentum (AM) redistribution in the galaxy will produce MT, allowing the gas to flow in and to reach the center of the system. Due to the nature of the studied system, the sources of AM variations are related to gravitational forces and pressure gradients, namely,

$$\vec{\tau}_G = \vec{r} \times \nabla\phi, \tag{4}$$

$$\vec{\tau}_P = \vec{r} \times \frac{\nabla P}{\rho}. \tag{5}$$

The gravitational ($\vec{\tau}_G$) and the pressure gradient ($\vec{\tau}_P$) torques will act as a source of AM transport in the galactic system and provide clues about the MT process in high-redshift galaxies.

Figure 3 shows the ratio τ_G/τ_P as a function of radius at different redshifts for our four simulations, with $\tau_i \equiv |\vec{\tau}_i|$. The data are smoothed over ~ 30 pc in radius. All our simulations show that pressure gradient torques tend to dominate above ~ 100 pc, with a clear domination at almost all radii at lower redshift. This is the consequence of two processes: shocks due to the large-scale gas infalling onto the DM halo central region, and shocks due to SN and AGN feedback. There are, however, some regions of gravity domination above ~ 100 pc. The pressure gradient domination is clearer at smaller radii. Only at high redshift, $z \gtrsim 9$, does gravity dominate the center of the system. In the case without SN feedback the gravitational torque has a contribution at smaller radii ($r \sim$ few tens of parsecs) compared with the SN feedback simulations. This is due to the higher mass concentration in this simulation. In summary, the combined effect of gravity and pressure gradients redistributes AM in the disk and triggers MT that feeds the central BH in these systems. We note that due to the mass
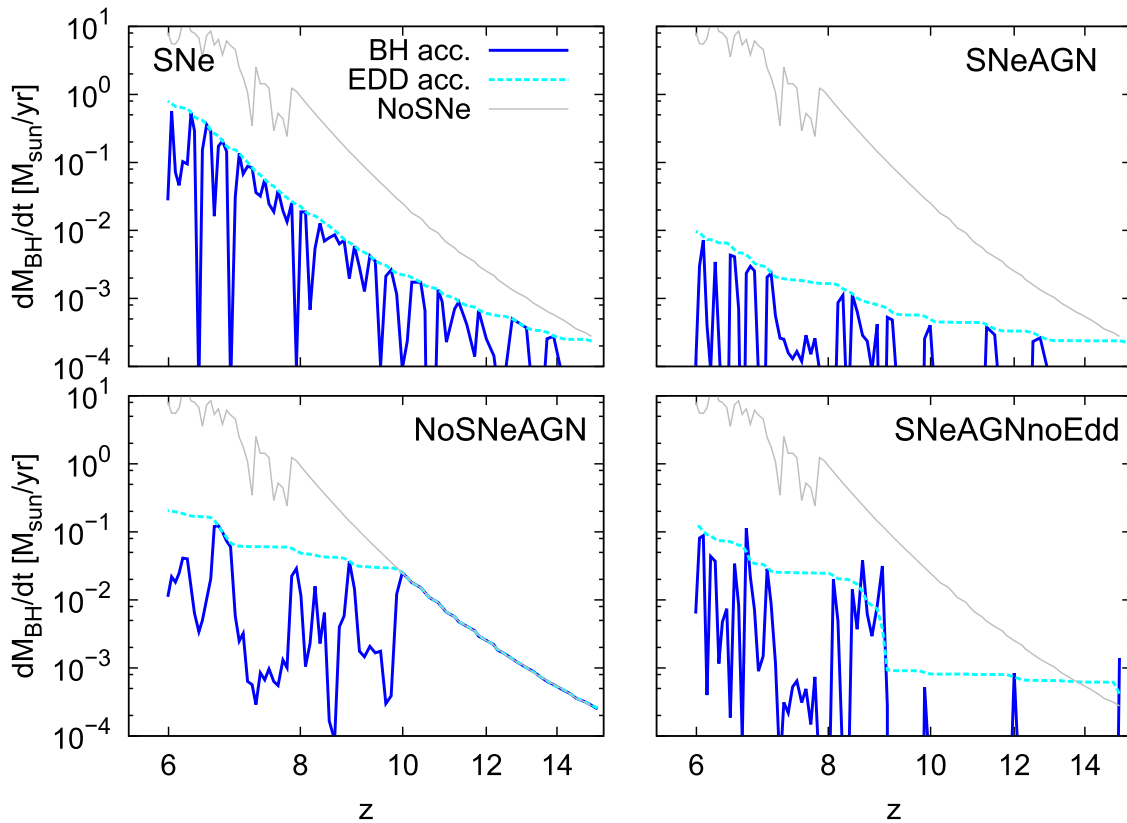
Figure 5. BH mass accretion rate for our four simulations as a function of redshift, shown with a solid blue line. The dashed cyan line marks the Eddington limit. For comparison, the solid gray line marks the BH accretion rate of the no-feedback NoSNe run in PE16. The top left panel clearly shows that SN feedback affects the mass accretion rate onto the BH. AGN feedback is able to reduce even more the accretion rate compared with the simulation with only SN feedback. The NoSNeAGN experiment allows a mass concentration in the galactic central region at high redshift, producing a practically Eddington-limited growth of the BH. The SNeAGNnoEdd run produces long periods of almost null accretion after super-Eddington episodes.

Table 1
Normalized BH Accretion Rates and BH Masses at $z = 10$ and $z = 6$

Simulation	$\langle f_{Edd} \rangle$	$\langle f_{Edd} \rangle$ $z > 10$	$\langle f_{Edd} \rangle$ $z < 10$	M_{BH} $(z = 6)$ $(M_\odot)$	M_{BH} $(z = 10)$ $(M_\odot)$
SNe	0.54	0.48	0.57	3.6×10^7	1.0×10^5
SNeAGN	0.24	0.14	0.30	4.3×10^5	2.0×10^4
NoSNeAGN	0.49	0.99	0.21	9.3×10^6	1.1×10^6
SNeAGNnoEdd	0.32	0.06	0.50	5.8×10^6	3.7×10^4

difference (above roughly one order of magnitude in the DM halo), our results do not completely agree with the ones presented in Danovich et al. (2015). Those authors show that the gravitational torque dominates on the galactic disk. As mentioned above, such a difference arises as a result of the larger mass of their studied systems at lower redshift.

3.2.2. Mass Accretion Rate in the Disk

As shown in the previous section, high-redshift galaxies receive almost freefalling material from large scales and experience torques associated with gravitational forces and pressure gradients that trigger MT in the galaxy. In this context, it is relevant to study and quantify the mass accretion rate in the galactic disk due to such phenomena and onto the central BH.

Figure 4 shows the radial gas mass accretion rate in the disk as a function of radius inside $\sim 0.1 R_{vir}$ at different redshifts for our four runs. We defined the mass accretion in the disk as

$$\frac{dM_g}{dt} = -2\pi r \Sigma_g v_r. \quad (6)$$

We first compute the gas AM vector inside a radius $r = 0.1 R_{vir}$ and take it as the $\hat{z}$ vertical axis of the cylindrical coordinate system of reference. The cylindrical radial coordinate r is defined in the disk plane perpendicular to the AM vector, and both the gas surface density Σ_g and the radial velocity v_r are cylindrical shell averages in the $\hat{z}$ direction, up to a height such that 90% of the baryonic mass is enclosed.

All simulations show large fluctuations in the mass accretion rate, attesting to the dynamical conditions in these environments: large-scale gas inflows and SN feedback shock the gas, creating a turbulent environment. Accretion rates fluctuate between $\sim 10^2$ and $\sim 10^{-2}\ M_\odot\ yr^{-1}$, with an average accretion rate of the order of ~ 1–$10\ M_\odot\ yr^{-1}$. The accretion rate profiles
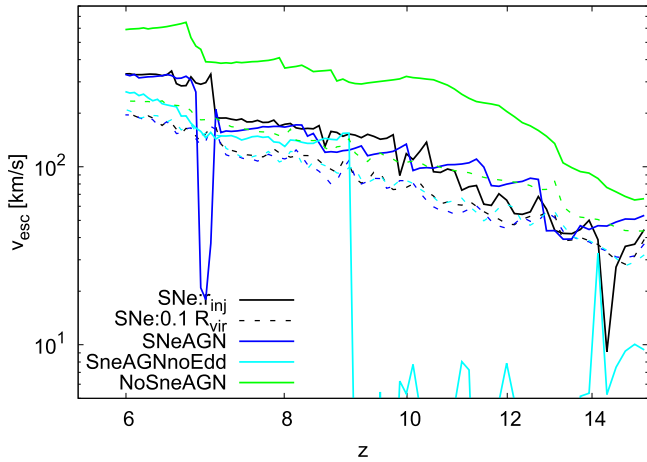
Figure 6. Escape speed at different distances from the BH as a function of redshift for our four simulations. The solid line marks the escape speed at the energy injection radius $r_{inj} = 4\Delta x_{min}$, and the dashed line that at $0.1R_{vir}$. Cases shown are SNe in black, SNeAGN in blue, SNeAGNnoEdd in cyan, and NoSNeAGN in green. Due to the lack of SN heating, the no-SN-feedback experiment has the higher escape speed: it allows much more mass concentration in the galaxy. On the other hand, the no-Eddington-limit case depletes the tiny galaxy of gas at high redshift after super-Eddington episodes, decreasing its escape speed.

show a number of gaps associated with SN outflows and gas clumps crossing and leaving the system.

The lack of SN heating in the NoSNeAGN simulation causes smoother accretion rate profiles compared with all the SN feedback simulations. Furthermore, in simulations with AGN feedback gas does not easily reach the central galactic region, $r \lesssim 10$ pc, i.e., AGN feedback efficiently ejects gas from the galactic center, as we will discuss in the next section.

3.3. BH Evolution

We have shown that after to inflow from scales above $\sim R_{vir}$ and reach the galactic outer region, the gas experiences gravitational and pressure gradient torques which produce a substantial mass accretion rate of the order of $\sim(1–10)\,M_\odot\,\mathrm{yr}^{-1}$ at distances greater than or approximately a few tens of parsecs from the center of the system in high-redshift galaxies. We now move on to explore the BH mass growth and how dynamical features of the system depend on SN and AGN feedback.

3.3.1. BH Accretion Rate

We show the BH accretion rate as a function of redshift in Figure 5. As already shown by PE16, the SN explosions have a clear effect on the central BH mass accretion rate, ejecting gas out of the system and then decreasing the amount of material that can feed the BH throughout the simulation (see also Dubois et al. 2015). This is especially important at $z > 10$, when the halo mass is $\lesssim 10^9\,M_\odot$ and the stellar mass is $\lesssim$ few times $10^7\,M_\odot$. Under such conditions SN explosions can accelerate a fraction of the central galactic gas beyond the local escape velocity, considerably reducing the amount of gas in the BH neighborhood. The SN run is characterized by intermittent Eddington-limited accretion episodes with an average $\langle \dot{M}_{BH}/\dot{M}_{Edd} \rangle \equiv \langle f_{Edd} \rangle \approx 0.54$ and a final BH mass $M_{BH} \approx 3.6 \times 10^7\,M_\odot$ (see Table 1).

AGN and SN feedback in tandem (SNeAGN) reduces significantly the mass accretion rate, a factor of ~ 2 overall, with $\langle f_{Edd} \rangle \approx 0.24$ and a final BH mass $M_{BH} \approx 4.3 \times 10^5\,M_\odot$.

Besides the SN energy injection, the local effect of the AGN activity is able to eject the already low amount of gas from the galactic center, reducing dramatically the mass accretion rate. Notwithstanding, the central BH has a number of Eddington-limited episodes.

The NoSNeAGN run shows an interesting behavior. Early on the BH accretes close to the Eddington limit as in the no-SN-feedback case of PE16 (see the gray solid line in Figure 5). This behavior continues to $z \sim 10$, when the now sufficiently massive BH is capable of accelerating the surrounding gas beyond the central escape velocity. The lack of SN heating allows the gas to easily reach the galactic center and pile up to feed the BH. At the same time, the accumulation of gas deepens the potential well and increases the central escape velocity, as shown in Figure 6, making it difficult for gas affected by AGN feedback to leave the central region. At $z \sim 10$, the BH mass has grown enough that AGN feedback becomes sufficiently strong to quench BH accretion (see the bottom left panel in Figure 5). Overall, the mean accretion rate, $\langle f_{Edd} \rangle \approx 0.49$, and final BH mass, $M_{BH} \approx 9.3 \times 10^6\,M_\odot$, are in between the case with only SN feedback and that with both SN and AGN feedback.

SNeAGNnoEdd, the case without Eddington limit but with both types of feedback included, is characterized by an early peak of super-Eddington accretion at $z \sim 15$. This early burst, in a tiny galaxy, causes catastrophic feedback that essentially shuts off accretion until $z < 10$. It is important to note that feedback has not been modified to take into account the lower radiative efficiency expected in super-Eddington accretion disks (see Volonteri et al. 2015, and references therein; a simulation following such a scenario is work in progress and will be part of an upcoming paper). A lower radiative efficiency decreases the injected energy from feedback (see Equation (1)) and would be less disruptive on its surroundings (Lupi et al. 2016). In this case the average $\langle f_{Edd} \rangle$ is ≈ 0.32, with a final mass $M_{BH} \approx 5.8 \times 10^6\,M_\odot$.

Table 1 shows $\langle f_{Edd} \rangle$ for all our simulations, for the whole duration of the simulation, as well as only at $z > 10$ and $z < 10$ to highlight the effects described above. In all simulations including SN feedback, the high-redshift ($z > 10$) $\langle f_{Edd} \rangle$ is lower than the low-redshift ($z < 10$) $\langle f_{Edd} \rangle$. Between redshift 6 and 10 the system has become more massive and SN feedback alone cannot unbind the gas. In the simulation without SN feedback but with AGN feedback, the mean Eddington ratio is higher at higher redshift ($z > 10$): AGN feedback affects the BH accretion rate only when the BH has become sufficiently massive to drive powerful outflows and clear its immediate surroundings.

3.3.2. Dynamical Conditions

These simulations show how important outflows are on the dynamics of the central region of high-redshift galaxies. Depending on their power, they can change the mass distribution around the BHs and affect the dynamical conditions by changing the local escape velocity. Figure 6 shows the escape speed for our four simulations at different radii as a function of redshift. The escape speed from a given radius R is defined by $v_{esc} = \sqrt{2GM(<R)/R}$, with $M(<R)$ the total mass (BH, gas, stars, and DM) inside a radius R. The NoSNeAGN simulation has the largest escape speed at the injection radius $r_{inj} = 4\Delta x_{min}$ (solid green line; this is the velocity needed for the gas to leave the region from which the
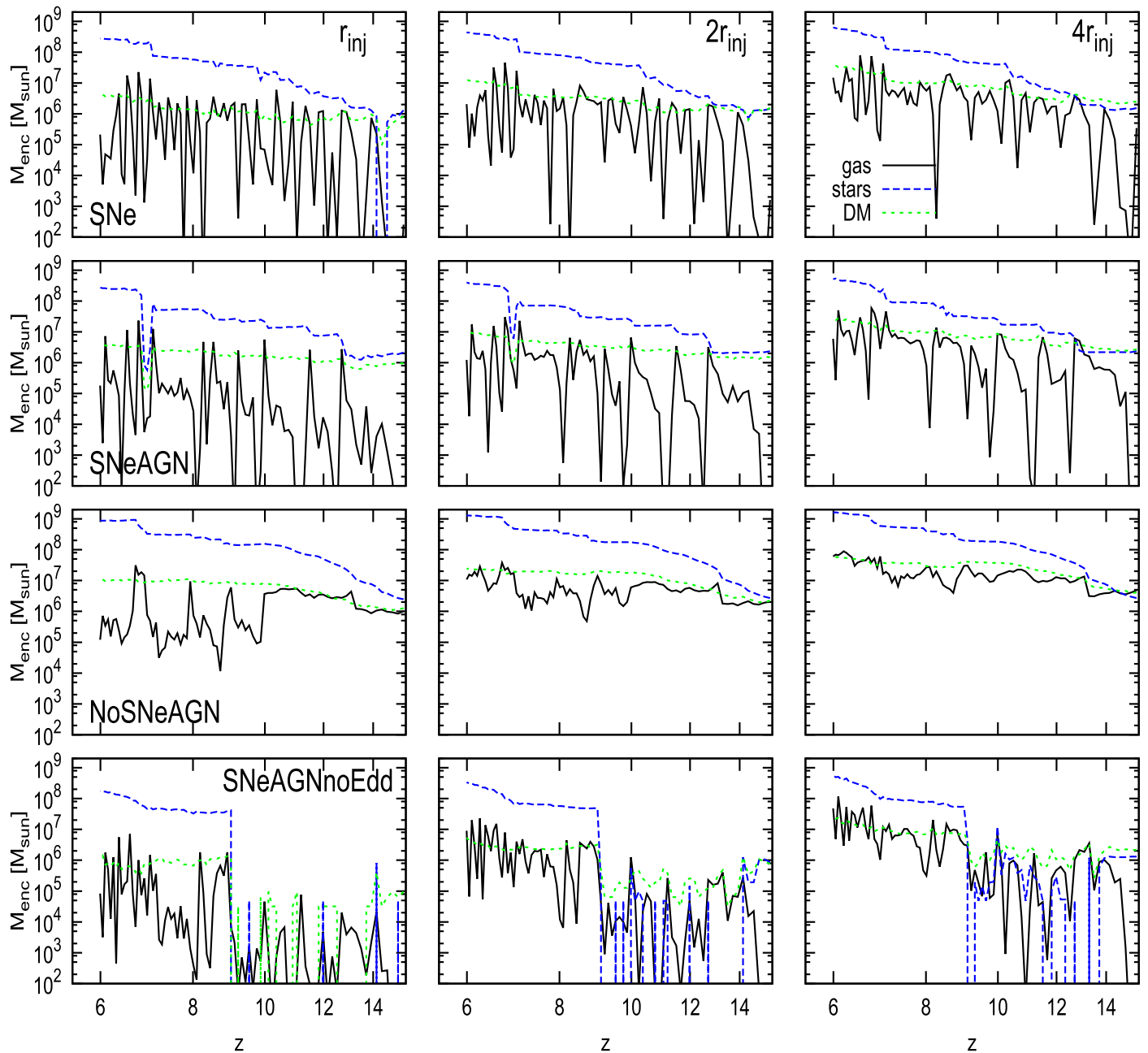
Figure 7. Enclosed mass of gas (solid black line), stars (long-dashed blue line), and DM (short-dashed green line) inside three different distances from the BH position in different columns. Each row shows the enclosed mass for each simulation as a function of redshift. The no-SN-feedback simulation has the highest central mass concentration at high redshift. In contrast, the no-Eddington-limit run has the lowest one. All the SN feedback simulations show an irregular behavior in the central gas content as a consequence of the regular gas mass removal. In all our simulations the central galactic region is dominated by the stellar mass, except in the no-Eddington-limit case, where the strong early feedback expels the nuclear gas and suppresses the star formation efficiently.

BH accretes, not for gas to leave the galaxy or the halo) and at $0.1R_{vir}$ (dashed green line; this can be considered the velocity needed to leave the galaxy). Due to the lack of SN heating, cold dense gas can pile up in the galaxy and in the BH vicinity, increasing the escape velocity. Such conditions clearly favor a high accretion rate onto the BH until it reaches a sufficiently high mass for its AGN activity to impact its surroundings.

In contrast, the SNeAGNnoEdd simulation has the lowest escape speed above $z \approx 9$ at the injection radius. In this case the strong AGN feedback associated with the early bursts at super-Eddington rates expels the gas around the BH, creating a very low density environment with a low escape speed (see bottom right panel of Figure 5), which favors mass depletion in

the BH vicinity and keeps the accretion to minimal levels. At $z \approx 9.5$ the escape speed increases at similar (but still lower) values compared with the other runs. At this redshift the main DM halo merges with a galaxy that has not been affected by AGN activity, increasing the enclosed central mass and consequently the escape velocity.

The SNe and SNeAGN runs show similar escape speeds at $0.1R_{vir}$. Their escape speeds have clearer differences at the injection radius. They fluctuate as a result of the SN and BH energy injection, which in both cases heats up and reduces the amount of available gas in the galactic center. Despite the similar escape speed in these two simulations, their BH growth is rather different (see Figure 5). In these simulations the mass
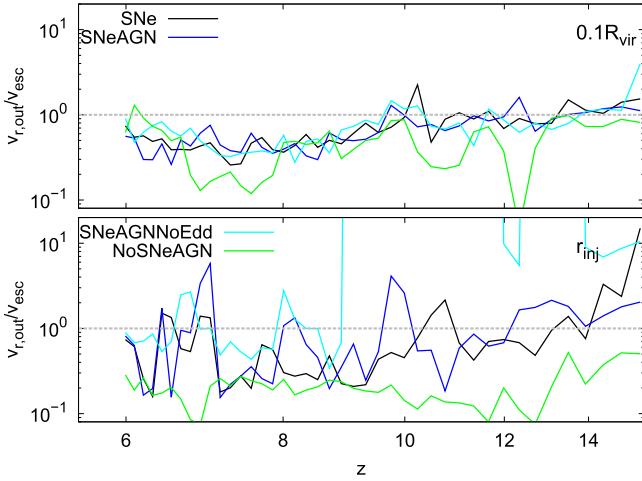
Figure 8. Outflow radial velocity normalized to the escape speed at different radii: $0.1R_{vir}$ (top) and r_{inj} (bottom). All ratios are smoothed over $\sim$20–30 Myr. Ejection of gas from the galaxy (with $0.1R_{vir}$ as a proxy) is intermittent and not very frequent. Near the BH (r_{inj}), the no-SN-feedback simulation has the lowest velocity ratio, meaning that gas is retained in the center, while the simulation without Eddington limiter retains no central gas.

inside r_{inj} is dominated by the stellar component, while accretion depends on gas content around the BH (as we will discuss later), which shows rapid and large fluctuations early on for simulations including SN feedback (Dubois et al. 2015). In the SNeAGN simulation, besides the SN mass outflows, AGN feedback is also at work, reducing substantially the BH growth rate compared with the BH mass accretion rate in the SN-only simulation.

Figure 7 shows the enclosed mass of gas, stars, and DM as a function of redshift for all simulations at three different distances from the BH position, namely, r_{inj}, $2r_{inj}$, and $4r_{inj}$. In all these simulations baryons dominate the enclosed mass in the BH vicinity, with a major contribution from the stellar component as mentioned above. This figure can explain why the SNeAGN experiment has a lower BH accretion rate compared with the only-SN-feedback run despite their escape speed being similar: the gas content around the BH in the AGN feedback simulation is lower than the one around the BH in the SN-only simulation. Only the no-Eddington-limited experiment shows that DM dominates the central galactic region at high redshift, $z \gtrsim 9$. In this particular case, the extreme BH feedback is strong enough to expel the central galactic gas and inhibit star formation.

Figure 8 shows the average mass-weighted gas outflow speed normalized by the escape speed, $v_{r,out}/v_{esc}$, as a function of redshift for our four simulations at two different radii, namely, $0.1R_{vir}$ and r_{inj}. The data are smoothed over $\sim$20–30 Myr. The dashed gray line shows $v_{r,out}/v_{esc} = 1$. At the injection radius the NoSNeAGN feedback simulation (green line) creates outflows with speeds well below the escape speed, due to the high mass concentration (see Figure 7) around the BH as mentioned above. At larger radii all the SN feedback simulations have an approximately similar behavior, showing that the stronger effects can be seen in the BH vicinity.

The run without Eddington limit (cyan line) produces nuclear outflows with speeds well above the escape speed at $z \gtrsim 9.5$ ejecting most of the gas around the BH and quenching efficiently BH growth and central star formation. The combined effect of gas ejection and reduced star formation decreases the central mass concentration, reducing the escape velocity. Under

such conditions, feedback can easily unbind the gas, and only the merger at $z \sim 9.5$ increases the central mass at levels comparable with the other SN simulation runs.

The SNe and SNeAGN simulations have a similar behavior in the innermost region of the galaxy. These simulations have a highly fluctuating behavior with periods of bound and unbound central gas, which is reflected in the BH mass accretion rate in Figure 5; however, the nature of the gas that is accelerated in both cases is different, as we will see below.

3.4. Velocity Distribution in the Galactic Gas

Figure 9 shows the average mass inside radial outflow velocity bins for gas inside $0.01R_{vir}$ colored by the ratio t_{cool}/t_{rad}. The mass in each velocity bin is averaged over a time interval $\Delta t \approx 220$ Myr, and they are shown for three different redshift intervals, namely, $15 > z > 10$, $10 > z > 7.5$, and $7.5 > z > 6$. The cooling timescale is defined as $t_{cool} = U/(n_H \Lambda)$, where $U = 3nk_B T/2$ is the gas internal energy and Λ is the gas cooling function, that is, a function of both T, the gas temperature, and Z, the gas metallicity. The radial timescale is defined as $t_{rad} = r/v_r$, where r is the radial coordinate and v_r is the gas outflow radial velocity with respect to the BH motion. The origin of the system is set at the BH position. The left column of Figure 9 shows the hot ($T > 10^6$ K) gas, and the right column shows the cold ($T < 5 \times 10^4$ K) gas. The black solid line marks the 1D velocity dispersion σ_{gas} of the NoSNe simulation averaged over Δt. This velocity dispersion gives us an idea about an outflow turbulent velocity triggered only by gravitational processes. In general, the feedback simulations presented here develop outflows with $v_r \gtrsim 2\sigma_{gas}$.

When we look at the hot gas at high redshift, $z > 10$, the NoSNeAGN run produces slower hot gas compared with all the SN feedback simulations. In this case the AGN activity cannot accelerate the hot galactic gas above $\sim$400 km s^{-1}. In other words, without the SN heating the hot gas cannot be accelerated above this velocity during the Eddington-limited growth phase of the BH. SN feedback can create a low-density rarefied hot environment where energy injection from SNe (and AGN feedback for the SNeAGN run) can easily accelerate the gas. In contrast, without SN feedback, the heated gas is surrounded by high-density gas, and it is much more difficult to accelerate it at higher velocities. We note that this fast hot gas is no more than a few percent of the total enclosed gas mass. Note that this result differs quantitatively, but not qualitatively, from Costa et al. (2015) because they simulate a more massive halo of $3 \times 10^{12} M_\odot$ at $z = 6$ powering a luminous quasar, while the halo in our simulations is of much lower mass, $3 \times 10^{10} M_\odot$, and AGN feedback remains weak and its effect limited.

In the cold gas phase, clear differences exist between our experiments. Without AGN feedback, cold gas cannot be accelerated above $\sim$150–200 km s^{-1}, as shown also by Costa et al. (2015). The inclusion of AGN feedback can accelerate cold gas to higher velocities, up to $\sim$300 km s^{-1} for the case without SNe and up to $\sim$500 km s^{-1} for the case with both SN and AGN feedback. This confirms, in a different regime, that the combined effects of SN and AGN feedback boost each other and are what accelerates the cold gas: the AGN accelerates the gas further than it has been already accelerated by SNe. Finally, note that the large timescale ratios t_{cool}/t_{rad} for
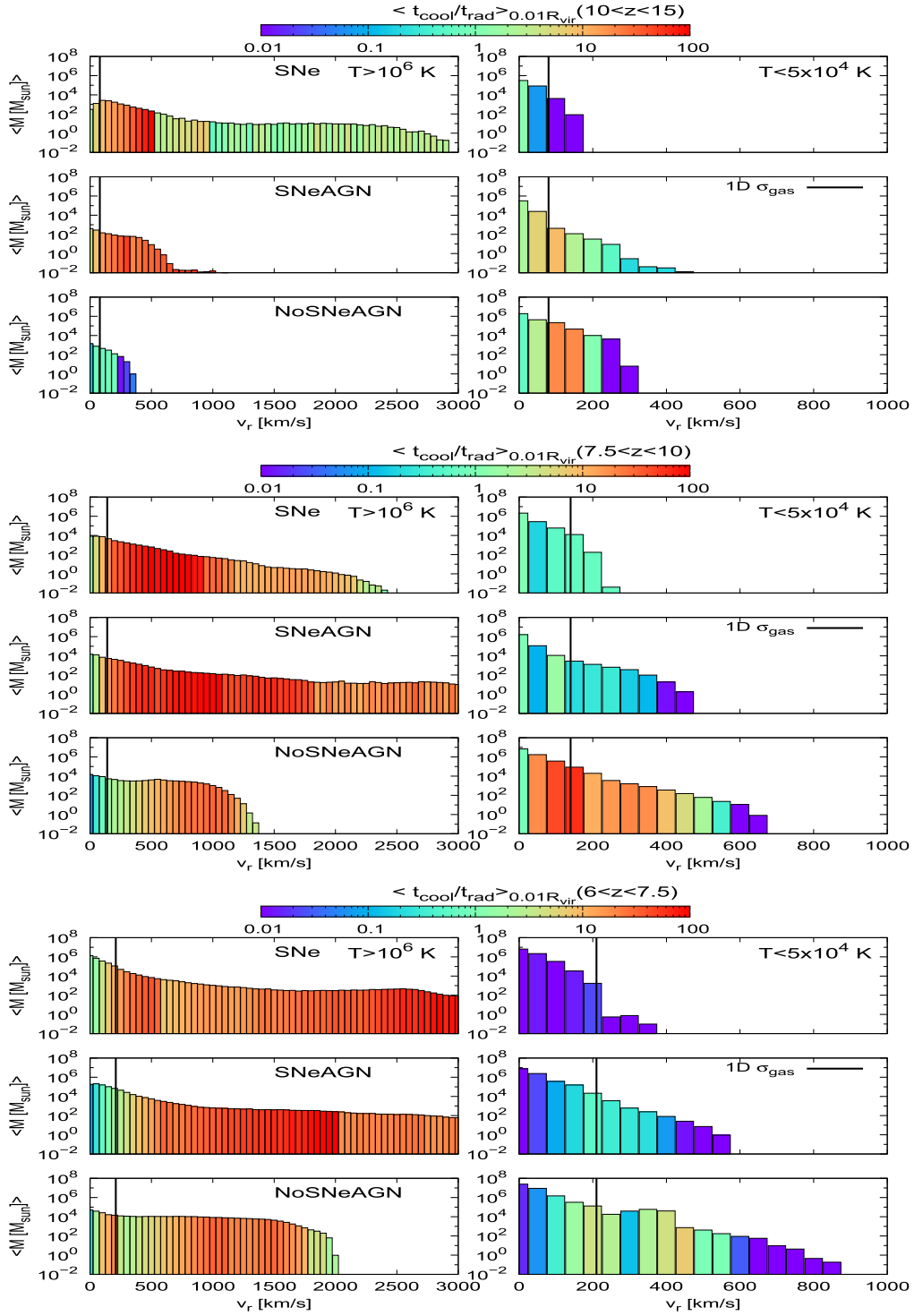
Figure 9. Average mass inside radial outflow velocity bins colored by the ratio of average cooling time to radial time $\langle t_{cool}/t_{rad} \rangle$ for three of our simulations inside $0.01R_{vir}$. The left column shows the hot ($T > 10^6$ K) gas, and the right column shows the cold ($T > 5 \times 10^4$ K) gas. The three panels are the average PDFs for three different time intervals $\Delta t \approx 220$ Myr from $z \approx 15$ to $z = 6$. The black solid line marks the 1D gas velocity dispersion averaged over Δt in the case of no feedback, NoSNe. See the text for discussion.

the NoSNeAGN run are caused by the lack of metal enrichment.

In the redshift interval $7.5 < z < 10$ the picture remains similar, but the now more massive BHs produce a more efficient AGN feedback, especially on the cold gas. This efficiency increases with time, and at $6 < z < 7.5$ the NoSNeAGN simulation shows hot gas outflows up to

$\sim$2000 km s^{-1}, but not beyond, in contrast with all the cases including SN feedback, which go as high as $\sim$3000 km s^{-1}. In the cold gas phase, SNe alone become completely ineffective at accelerating the cold gas, and it is only in the presence of an AGN that cold gas can be affected in the now massive galaxy (see the discussion in Dubois et al. 2015). Additionally, in the SN-only case, $\langle t_{cool}/t_{rad} \rangle \sim 0.01$ for the cold gas at
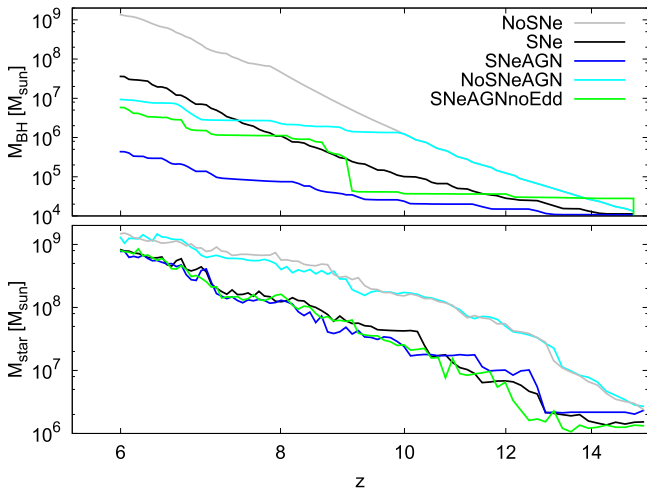
Figure 10. BH mass (top) and stellar mass (bottom) as a function of redshift for our four simulations. Cases shown are SNe in black, SNeAGN in blue, NoSNeAGN in cyan, and SNeAGNnoEdd in green. The gray solid line in the top panel shows the BH mass in the no-feedback simulation NoSNe of PE16. The NoSNeAGN run clearly forms more stars, comparable to the NoSNe simulation in PE16.

$6 < z < 7.5$, while time ratios of order $\lesssim 1$ are present in the simulations including AGN feedback.

The cold gas in the no-Eddington-limit simulation (not shown) can surpass the ~ 500 km s^{-1} during super-Eddington accretion episodes at redshift above 10. Below $z = 10$ the outflows can reach ~ 1000 km s^{-1} during super-Eddington episodes. Those episodes, however, are very short-lived and are followed by long quiescent periods; therefore, the outflow velocity, averaged over hundreds of megayears, remains low.

Note that inside $0.01R_{\mathrm{vir}}$ the mass of hot gas is much lower than the mass of cold gas in our simulations. At $z > 10$ hot gas is not more than few percent of the total gas mass inside 1% of the virial radius, increasing to a few percent at $7.5 < z < 10$. In the final redshift range, $6 < z < 7.5$, all the simulations including SN feedback reach values in the range of $\sim 10\%$–25%. The NoSNeAGN feedback remains at $\sim 1\%$ of hot gas and is the case with the lowest hot gas fraction also in the previous redshift intervals.

3.4.1. BH and Stellar Mass Evolution

The discussion on the BH accretion rate and gas velocities presented in the previous sections now allows us to understand the BH and stellar mass evolution in this high-redshift galaxy. Figure 10 shows the BH and galaxy stellar mass evolution as a function of redshift. The SN simulation (black) reaches the highest BH mass at the end of the experiment (except for the run with no feedback at all, described in PE16 and reported here for comparison). SN feedback can accelerate the gas because of pressure gradients associated with temperature differences of the order $\Delta T \sim 10^{5-6}$ K (depending on the gas density) in the galactic disk.

As shown in the bottom left panel of Figure 5, due to the high mass concentration around the BH (and its high escape velocity), the BH in the NoSNeAGN case has the fastest growth at high redshift among all our simulations, comparable with the no-feedback case of PE16. As shown in Table 1, the BH grows at the Eddington rate at $z > 10$, until it reaches $M_{\mathrm{BH}} \approx 10^6 M_\odot$. At this stage AGN feedback is capable of accelerating the surrounding gas beyond the central escape

velocity, reducing dramatically the BH growth rate. The BH ends the simulation with a mass of $M_{\mathrm{BH}} \approx 9 \times 10^6 M_\odot$.

At the beginning of the evolution, the SNeAGNnoEdd BH shows a large mass jump, increasing almost by three times its initial value, due to short bursts of super-Eddington accretion accompanied by strong feedback. Afterward, as discussed in the previous sections, the central region is devoid of gas and BH growth is stunted until a merger at $z \sim 9.5$ that replenishes the gas supply and the BH experiences a high super-Eddington accretion ($f_{\mathrm{EDD}} \lesssim 10$) episode, increasing its mass by almost one order of magnitude. By this time, however, AGN feedback is not as disruptive anymore in the denser and more massive nucleus, and the BH continues its evolution with irregular mass accretion rate and with more super-Eddington episodes.

The SNeAGN feedback has the slowest mass growth, and then it reaches the lowest mass at the end of the simulation ($M_{\mathrm{BH}} \approx 4 \times 10^5 M_\odot$.) In this case, besides the SN outflows, AGN activity can create outflows associated with temperature gradients of $\Delta T \gtrsim 10^7$ K, much larger than the ones produced by SNe. This result shows that the combined effect of SN and AGN feedback works together to quench efficiently the BH growth.

At $z \approx 7$ all the simulations including AGN feedback (SNeAGN, NoSNeAGN, and SNeAGNnoEdd) show a sudden change in the BH mass. At this redshift the system experiences a 1: 3 merger, bringing fresh high-density gas to the central galactic region to fuel the BH. Figure 11 shows two episodes of rapid BH mass growth for the SNeAGN simulation, one at $z \approx 13$ and another at $z \approx 7$ (mentioned above). In these two examples it is possible to associate a merger event with a jump in the BH mass evolution (see Dubois et al. 2015).

Regarding the stellar mass evolution, the simulation with no SNe and only AGN feedback, NoSNeAGN, produces the galaxy with the highest stellar mass at the end of the simulation, comparable to but lower than the NoSNe run in PE16. The final stellar mass is $M_\star \approx 1.5 \times 10^9 M_\odot$. As expected, the lack of fast outflows allows high gas concentration and therefore an efficient star formation throughout the simulation. In contrast, all the cases including SN feedback finish the simulation with a lower stellar mass, of the order of $M_\star \approx 8 \times 10^8 M_\odot$, showing that the BH mass is not large enough in these galaxies to quench star formation.

All the SN feedback simulations have similar stellar masses at $z < 8$, $M_\star > 10^8 M_\odot$. Above this redshift it is possible to see that the stellar masses differ. In other words, it seems that below $M_\star \sim 10^8 M_\odot$ SN and AGN feedback produces a larger scatter in the stellar mass content at similar DM halo masses.

4. Discussion and Conclusions

We have run cosmological zoom-in simulations of high-redshift galaxies in order to study the effects of SN and AGN feedback on the MT in these objects and their consequences on the central BH growth.

As in PE16, we find that the mass accretion rate beyond the virial radius is of the order of $\sim 10 M_\odot$ yr^{-1}. These high mass accretion rates are associated with material in almost freefall going onto the central DM halo region. In these systems, feedback from SNe and AGNs is able to suppress the low-density mass accretion at the galactic edge. Material with densities associated with cooling flows, i.e., $n \lesssim 0.1$–1 cm^{-3}, cannot penetrate inside the central ~ 1 kpc. Only high-density ($n \gtrsim 10^2$ cm^{-3}) gas is able to reach the inner roughly few
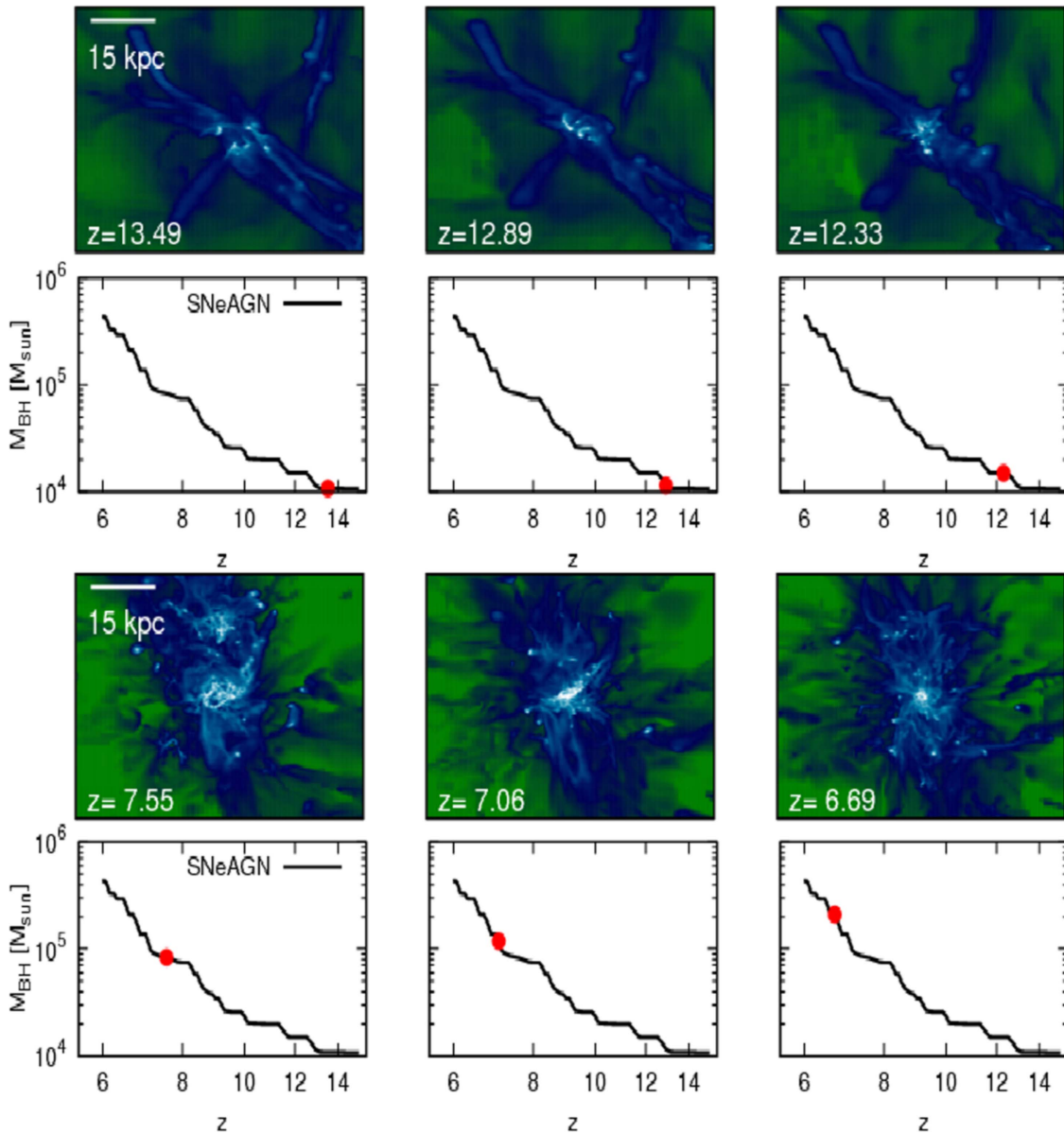
Figure 11. Gas maps (from top to bottom, the first and third rows) and BH mass evolution (from top to bottom, the second and fourth rows) as a function of redshift for the SNeAGN run. The figure shows the BH mass evolution at different redshifts marked with red circles. These are two examples of the connection between merger events and rapid BH growth in our simulation.

hundred parsecs. The simulations with only SN feedback and the simulation with SN plus AGN feedback are those for which the suppression is the highest, in contrast to the AGN-only experiment, where gas can reach the galactic center more easily.

In these turbulent galactic environments, torques acting on the gas have two sources: gravity force associated with an inhomogeneous mass distribution, and pressure gradients associated with circumgalactic shocks driven by cosmic infall, or SN and AGN feedback. Such torques are required to redistribute the gas AM from the external edge of the galaxy to the central regions, at roughly parsec scales, and trigger a radial mass accretion rate of $\dot{M} \sim 1\ M_\odot\ \mathrm{yr}^{-1}$.

All the SN feedback simulations produce a lower $\langle f_{\mathrm{EDD}} \rangle$ at $z > 10$ compared with their $\langle f_{\mathrm{EDD}} \rangle$ at $z < 10$, showing that SN feedback can efficiently quench BH growth in small galaxies at high redshift until a critical mass is reached (Dubois et al. 2015). Furthermore, it is possible to see that after merger

events, the BH has a significant growth. During such events, a large amount of gas reaches the BH, feeding it with fresh gas.

Our four simulations show very different BH mass accretion histories depending on the physical ingredients we included. Although SN feedback alone is able to alter dramatically the BH accretion rate (Dubois et al. 2015; Habouzit et al. 2016, and PE16), the SN and AGN feedback in tandem is the most efficient way to quench the BH growth. Due to the high gas density around the BH at high redshift, the simulation without SN feedback can grow near the Eddington limit until it reaches $M_{\mathrm{BH}} \sim 10^6\ M_\odot$ and self-regulates by its AGN activity.

Regarding stellar mass growth, AGN feedback alone is also unable to regulate star formation, although the ratio of BH to stellar mass is large; in fact, for the noSNeAGN case, the ratio is well above 10^{-3} at almost all times. SN feedback, in these small galaxies, seems to be much more effective at affecting star formation.

Our simulations show that most of the central gas inside 1% of the halo virial radius is cold ($T < 5 \times 10^4$ K). The hot ($T > 10^6$ K) gas is no more than a few percent above redshift $z \gtrsim 7.5$. Below this redshift, all the simulations including SN feedback increase the amount of hot gas reaching fractions $\lesssim 10\%$–25%. In contrast, the no-SN-feedback simulation keeps its hot gas fraction very low, $\lesssim 1\%$, over its entire evolution.

The simulation without SN feedback shows that it is not possible to accelerate the hot gas beyond 2000 km s^{-1}. In contrast, all the SN feedback simulations can easily surpass this value, showing that SN heating creates a low-density rarefied gas where the SN and AGN feedback accelerates the gas at velocities as high as 3000 km s^{-1}.

The cold gas phase in the innermost galactic region of the SN feedback simulation cannot be accelerated beyond $\sim$150–200 km s^{-1} (Costa et al. 2015), whereas with AGN plus SN feedback the cold gas can reach up to $\sim$500 km s^{-1}, showing that the combined effect of SN and AGN heating creates the strongest outflows of cold gas and consequently is the most efficient combination to quench the BH and galaxy growth at high redshift.

We note that our results should depend on the BH feedback prescription. In particular, a more realistic approach based on a quasar and radio-jet-like mode as in Dubois et al. (2012) would produce a lower effect on the surrounding gas, increasing the BH growing rate and reducing the gas outflow velocity. A simulation including a jet like BH feedback will be presented in an upcoming paper.

References

Abel, T., Bryan, G. L., & Norman, M. L. 2002, Sci, 295, 93
Agarwal, B., Khochfar, S., Johnson, J. L., et al. 2012, MNRAS, 425, 2854
Arribas, S., Colina, L., Bellocchi, E., Maiolino, R., & VillarMartín, M. 2014, A&A, 568, A14
Bandara, K., Crampton, D., & Simard, L. 2009, ApJ, 704, 1135
Begelman, M. C., Rossi, E. M., & Armitage, P. J. 2008, MNRAS, 387, 1649
Begelman, M. C., Volonteri, M., & Rees, M. J. 2006, MNRAS, 370, 289
Biernacki, P., Teyssier, R., & Bleuler, A. 2017, arXiv:1701.05190
Bleuler, A., & Teyssier, R. 2014, MNRAS, 445, 4015
Bondi, H. 1952, MNRAS, 112, 195
Booth, C. M., & Schaye, J. 2009, MNRAS, 398, 53
Bower, R., Schaye, J., Frenk, C. S., et al. 2016, arXiv:1607.07445
Choi, J., Shlosman, I., & Begelman, M. C. 2015, MNRAS, 450, 4411
Clark, P. C., Glover, S. C. O., Smith, R. J., et al. 2011, Sci, 331, 1040
Costa, T., Sijacki, D., & Haehnelt, M. G. 2015, MNRAS, 448, L30
Dalgarno, A., & McCray, R. A. 1972, ARA&A, 10, 375
Danovich, M., Dekel, A., Hahn, O., Ceverino, D., & Primack, J. 2015, MNRAS, 449, 2087
De Rosa, G., Venemans, B. P., Decarli, R., et al. 2014, ApJ, 790, 145
Devecchi, B., Volonteri, M., Rossi, E. M., Colpi, M., & Portegies Zwart, S. 2012, MNRAS, 421, 1465
Di Matteo, T., Croft, R. A. C., Feng, Y., Waters, D., & Wilkins, S. 2016, arXiv:1606.08871
Di Matteo, T., Khandai, N., DeGraf, C., et al. 2012, ApJL, 745, L29
Dressler, A. 1989, in IAU Symp. 134, Active Galactic Nuclei, ed. D. E. Osterbrock & J. S. Miller (Dordrecht: Kluwer), 217
Dubois, Y., Devriendt, J., Slyz, A., & Teyssier, R. 2012, MNRAS, 420, 2662
Dubois, Y., Pichon, C., Haehnelt, M., et al. 2012, MNRAS, 423, 3616
Dubois, Y., & Teyssier, R. 2008, A&A, 477, 79
Dubois, Y., Volonteri, M., Silk, J., et al. 2015, MNRAS, 452, 1502
Fan, X., Strauss, M. A., Schneider, D. P., et al. 2001, AJ, 121, 54
Ferrarese, L., & Ford, H. 2005, SSRv, 116, 523
Ferrarese, L., & Merritt, D. 2000, ApJ, 539, 9
Gebhardt, K., Bender, R., Bower, G., et al. 2000, ApJL, 539, L13
Genzel, R., Förster Schreiber, N. M., Rosario, D., et al. 2014, ApJ, 796, 7
Ghez, A. M., Salim, S., Hornstein, S. D., et al. 2005, ApJ, 620, 744
Greif, T. H., Springel, V., White, S. D. M., et al. 2011, ApJ, 737, 75
Gültekin, K., Richstone, D. O., Gebhardt, K., et al. 2009, ApJ, 698, 198
Haardt, F., & Madau, P. 1996, ApJ, 461, 20
Habouzit, M., Volonteri, M., & Dubois, Y. 2016, arXiv:1605.09394
Haiman, Z. 2013, ASSL, 396, 293
Humphrey, A., Villar-Martín, M., Sánchez, S. F., et al. 2010, MNRAS, 408, L1
Katz, H., Sijacki, D., & Haehnelt, M. G. 2015, arXiv:1502.03448
Kormendy, J., & Richstone, D. 1995, ARA&A, 33, 58
Latif, M. A., Bovino, S., Van Borm, C., et al. 2014, MNRAS, 443, 1979
Latif, M. A., Schleicher, D. R. G., Schmidt, W., & Niemeyer, J. C. 2013, MNRAS, 436, 2989
Lodato, G., & Natarajan, P. 2006, MNRAS, 371, 1813
Lupi, A., Colpi, M., Devecchi, B., Galanti, G., & Volonteri, M. 2014, MNRAS, 442, 3616
Lupi, A., Haardt, F., Dotti, M., et al. 2016, MNRAS, 456, 2993
Magorrian, J., Tremaine, S., Richstone, D., et al. 1998, AJ, 115, 2285
Mortlock, D. J., Warren, S. J., Venemans, B. P., et al. 2011, Natur, 474, 616
Nesvadba, N. P. H., Polletta, M., Lehnert, M. D., et al. 2011, MNRAS, 415, 2359
Oh, S. P., & Haiman, Z. 2002, ApJ, 569, 558
Omukai, K., Schneider, R., & Haiman, Z. 2008, ApJ, 686, 801
Park, K., Ricotti, M., Natarajan, P., Bogdanović, T., & Wise, J. H. 2016, ApJ, 818, 184
Pichon, C., Pogosyan, D., Kimm, T., et al. 2011, MNRAS, 418, 2493
Planck Collaboration 2013, arXiv:1303.5076P
Powell, L. C., Slyz, A., & Devriendt, J. 2011, MNRAS, 414, 3671
Prieto, J., & Escala, A. 2016, MNRAS, 460, 4018 (PE16)
Prieto, J., Jimenez, R., Haiman, Z., & González, R. E. 2015, MNRAS, 452, 784
Prunet, S., Pichon, C., Aubert, D., et al. 2008, ApJS, 178, 179
Rasera, Y., & Teyssier, R. 2006, A&A, 445, 1
Schneider, R., Omukai, K., Inoue, A. K., & Ferrara, A. 2006, MNRAS, 369, 1437
Shakura, N. I., & Sunyaev, A. R. 1973, A&A, 24, 337
Stacy, A., Greif, T. H., & Bromm, V. 2010, MNRAS, 403, 45
Sutherland, R. S., & Dopita, M. A. 1993, ApJS, 88, 253
Teyssier, R. 2002, A&A, 385, 337
Teyssier, R., Moore, B., Martizzi, D., Dubois, Y., & Mayer, L. 2011, MNRAS, 414, 195
Teyssier, R., Pontzen, A., Dubois, Y., & Read, J. I. 2013, MNRAS, 429, 3068
Tremaine, S., Gebhardt, K., Bender, R., et al. 2002, ApJ, 574, 740
Truelove, J. K., Klein, R. I., McKee, Ch. F., et al. 1997, ApJL, 489, 179
Volonteri, M. 2010, A&ARv, 18, 279
Volonteri, M., Lodato, G., & Natarajan, P. 2008, MNRAS, 383, 1079
Volonteri, M., Madau, P., & Haardt, F. 2003, ApJ, 593, 661
Volonteri, M., Silk, J., & Dubus, G. 2015, ApJ, 804, 148
Willott, C. J., Delorme, P., Omont, A., et al. 2007, AJ, 134, 2435